Interplay between the magnetic and magneto-transport properties of 3D interconnected nanowire networks

Tristan da Câmara Santa Clara Gomes, Joaquín De La Torre Medina, Yenni G. Velázquez-Galván, Juan Manuel Martínez-Huerta, Armando Encinas, and Luc Piraux

Citation: Journal of Applied Physics **120**, 043904 (2016); doi: 10.1063/1.4959249
View online: https://doi.org/10.1063/1.4959249
View Table of Contents: http://aip.scitation.org/toc/jap/120/4
Published by the American Institute of Physics

Interplay between the magnetic and magneto-transport properties of 3D interconnected nanowire networks

Tristan da Câmara Santa Clara Gomes,[1] Joaquín De La Torre Medina,[2,a)] Yenni G. Velázquez-Galván,[3] Juan Manuel Martínez-Huerta,[1] Armando Encinas,[3] and Luc Piraux[1,b)]

[1]*Institute of Condensed Matter and Nanosciences, Université catholique de Louvain, Place Croix du Sud 1, B-1348, Louvain-la-Neuve, Belgium*

[2]*Instituto de Investigaciones en Materiales-Unidad Morelia, Universidad Nacional Autónoma de México, Antigua Carretera a Pátzcuaro No. 8701 Col. Ex Hacienda de San José de la Huerta, C. P. 58190, Morelia, Mexico*

[3]*División de Materiales Avanzados, Instituto Potosino de Investigación Científica y Tecnológica, A. C., Camino a la Presa 2055, 78216 San Luis Potosí, SLP, Mexico*

(Received 28 May 2016; accepted 9 July 2016; published online 25 July 2016)

We have explored the interplay between the magnetic and magneto-transport properties of 3D interconnected nanowire networks made of various magnetic metals by electrodeposition into nanoporous membranes with crossed channels and controlled topology. The close relationship between their magnetic and structural properties has a direct impact on their magneto-transport behavior. In order to accurately and reliably describe the effective magnetic anisotropy and anisotropic magnetoresistance, an analytical model inherent to the topology of 3D nanowire networks is proposed and validated. The feasibility to obtain magneto-transport responses in nanowire network films based on interconnected nanowires makes them very attractive for the development of mechanically stable superstructures that are suitable for potential technological applications. *Published by AIP Publishing.*
[http://dx.doi.org/10.1063/1.4959249]

I. INTRODUCTION

The three-dimensional (3D) nanowire (NW) networks are attractive nanodevice components due to their unique architectures and high degree of wire interconnectivity that could be beneficial for a wide range of applications in energy harvesting/storage systems,[1–5] electronic sensing devices and actuators,[6–8] catalysts,[9] electrochromic elements,[10] solar cells,[11] biosensor,[12] bio-analytical devices,[13,14] among others. Magnetic NW networks are also expected to play an important role in the development of next-generation multifunctional devices. For instance, high-aspect-ratio 3D nanostructures embedded in a dielectric matrix can be used to fabricate magnetic devices with controlled anisotropy and microwave absorption properties.[15] The 3D networks of magnetic NWs have also potential applications for the storage and logic operation of information carried and processed by domain walls flowing along them.[16] However, the fabrication of 3D nanoarchitectures is extremely complicated with conventional lithography techniques and so far lacks the commercial viability. On the contrary, template-assisted synthesis is a versatile bottom-up approach for low-cost, reliable, and large-scale fabrication of NW networks with controlled size, geometry, composition, and surface morphology. Typically, these 3D networks are obtained by simple electrochemical deposition within the hierarchical nanopores of a suitable template. So far, various 3D nanoporous templates have been used for this purpose, including silica templates,[17] diblock copolymers,[10] 3D alumina nanoporous hosts,[1,2,18] as well as track-etched polymeric membranes.[9,15] The latter approach is the most promising as dense networks of crossed cylindrical nanopores can be obtained through sequential polycarbonate (PC) film irradiation with energetic heavy ions at different incidence angles, followed by selective chemical etching of the ion-tracks within the polymer film.[19] The suitability of such 3D nanoporous polymer templates to form dense interconnected NW networks with tunable geometrical parameters in terms of NW size, density, and orientation opens up the possibility for a controlled synthesis of a large variety of complex 3D networks of high aspect-ratio nanostructures with different geometries and materials. In this work, we explore the advantages of using such nanoporous track-etched polymer membranes with intrinsic crossed nanochannels to form dense networks of 40 nm diameter crossed nanowires (CNWs) made of various magnetic metals. The interconnected CNWs architecture facilitates the ability to perform basic magneto-transport measurements and to investigate the interplay between electronic transport and magnetic properties. The combination of magnetostatic effects and magnetocrystalline (MC) anisotropy, together with the peculiar geometrical arrangements and suitable choice of material composition, enables for the design of 3D CNW networks with tunable static and dynamic magnetic properties. We show that the effective magnetic anisotropy and absorption frequency of Co CNW networks can be strongly modified using well-known mechanisms to modify their microstructure, such as the electrolyte pH.[20] The measured anisotropic magneto-resistance ratio for CNW networks is closely related to their magnetic properties and is consistent with a spatial average that results from all the NWs orientations in the membrane. These are very useful features for

a)Electronic mail: delatorre@iim.unam.mx
b)Electronic mail: luc.piraux@uclouvain.be

applications of magnetic CNW networks in magnetic memory, sensor, and logic devices. Besides, it was found that mechanically stable and self-supporting magnetic CNW networks are formed after chemical dissolution of the polymer membrane. Our approach demonstrates the suitability of such 3D nanoporous polymer templates with controlled pore structure parameters to form magnetic CNW networks with a large variety of geometries and material compositions, which opens up the possibility for a controlled synthesis of complex nanoarchitectures with tunable magnetic and magneto-transport properties.

II. EXPERIMENTAL

The 20 μm thick crossed nanoporous templates have been prepared by performing a sequential multi-step exposure of energetic heavy ions, at various angles with respect to the normal of the PC film surface. For the present study, a PC film was subjected to a first irradiation step over a wide angular range from −45° to +45° with respect to the normal axis of the PC surface [see Fig. 1(a)]. Next, as shown in Fig. 1(b), for the second irradiation step, the film was rotated in the plane by 90° and re-exposed to the same angular variable irradiation flux to form finally a complex 3D nanochannel network. In both irradiation steps, the standard deviation was ±5° maximum around the target maximum angle. Both irradiation steps with quasi-continuous angular variation are a key requirement to obtain highly interconnected porous networks. The latent tracks were chemically etched in a 0.5M NaOH aqueous solution at 70° C to form 40 nm diameter nanopores, following a previously reported protocol.[19] The as-prepared polymer membrane containing dense networks of 3D interconnected cylindrical nanopores[9,15] was designed with volumetric porosity of approximately 20%. In a second stage, the PC templates were coated on one side using an e-beam evaporator with a metallic Cr/Cu bilayer to serve as cathode during the electrochemical deposition. The thickness of the thin adhesion layer of Cr was 10 nm, while for a

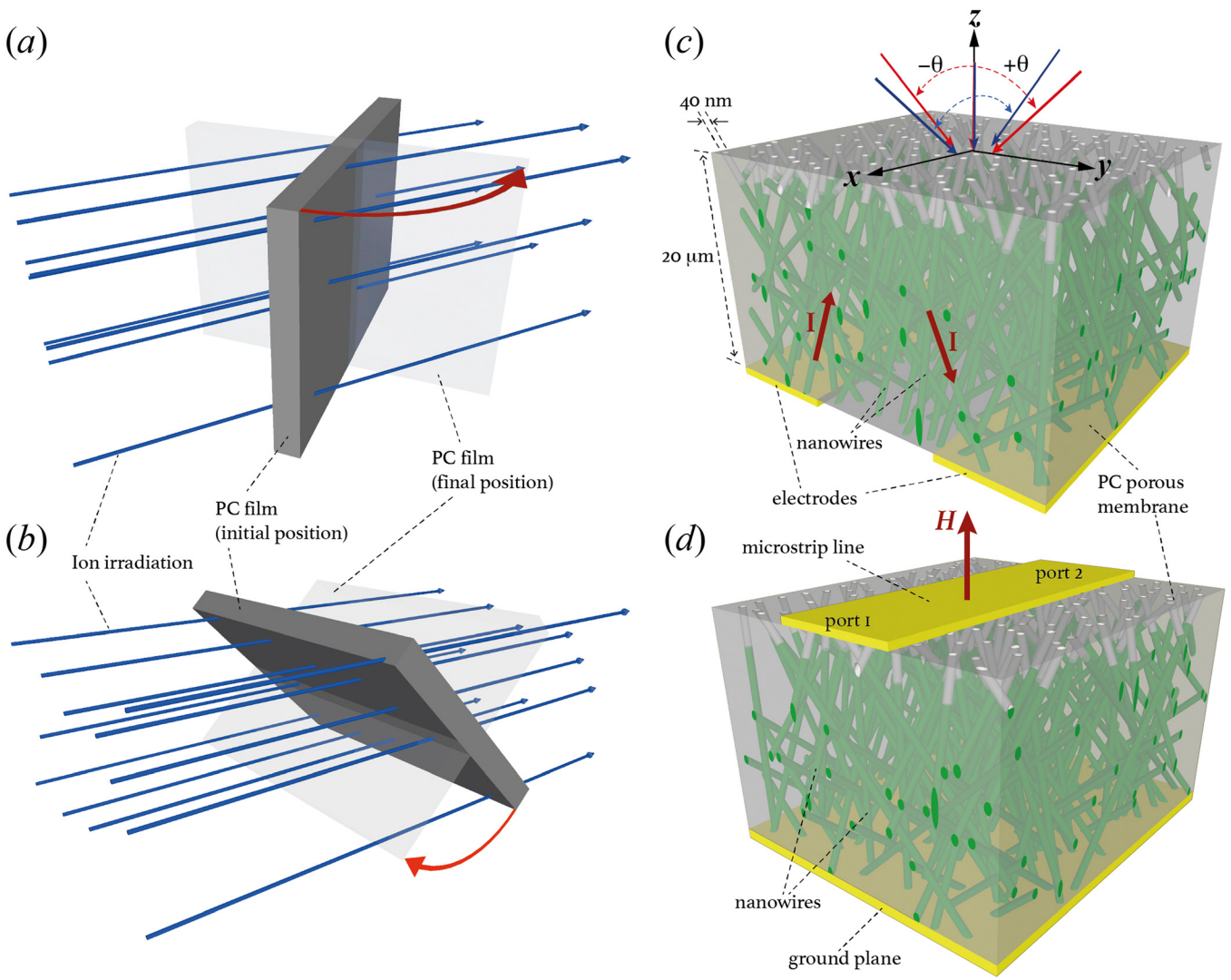

FIG. 1. Schematics of the track etching process (a) for the first irradiation step under an angular range of ±45° relative to the out-of-plane direction and (b) for the second irradiation step after in-plane PC membrane rotation by 90° and again under the same angular range relative to the OOP direction. (c) Schematic representation of a 3D PC template prepared by the successive irradiation steps of (a) and (b), featuring cylindrical nanopores with a mean diameter of 40 nm and partially filled with magnetic CNWs. An electrode design for two-probe electrical measurement obtained by local etching of the Cu cathode is also shown. (d) Schematic of a stripline transmission line for FMR measurement fabricated using similar partially filled membrane.

uniform and consistent nanopore coverage withstanding the electrodeposition process, the Cu film thickness was set to 150 nm.

Permalloy ($Ni_{80}Fe_{20}$) and Co CNW networks were grown by electrodeposition into crossed pore PC templates. All depositions were done at room temperature in the potentiostatic mode using a Ag/AgCl reference electrode and a Pt counter electrode. Electrodeposition of NiFe and Co CNWs was carried out at the respective constant potentials of −1 V and −0.95 V using the electrolytes: 5.5 g l^{-1} $FeSO_4$ + 131.4 g l^{-1} $NiSO_4$ + 30 g l^{-1} H_3BO_3 at pH 3; and 238.5 g l^{-1} $CoSO_4$ + 30 g l^{-1} H_3BO_3 in the pH range 2–6.4. The as-prepared Co solution has a pH value of 3.6, which was lowered gradually down to 2.0 by addition of diluted H_2SO_4 or increased up to 6.4 by addition of NaOH.[20] The morphology of the nanostructured CNW networks was characterized using a field-emission scanning electron microscope (FE-SEM). For the electron microscopy analysis, it was necessary to remove the PC template. This was done by first etching the Cr/Cu cathode using a I2:KI (0.1:0.6M) solution and then dissolving the polycarbonate with dichloromethane. X-ray diffraction (XRD) measurements have been carried out by using a Rigaku X-ray diffractometer with Cu $K\alpha_1$ radiation of wavelength $\lambda = 1.54$ Å. Magnetization curves were obtained at room temperature in the out-of-plane (OOP) and in-plane (IP) directions of the CNW network film, using an alternating gradient field magnetometer (AGFM-Lakeshore) with a maximum applied field of ±10 kOe. For the ferromagnetic resonance (FMR) measurements, a microstrip line wave-guide configuration has been used [Fig. 1(d)].[15,21] A 500 μm wide and 500 nm thick microstrip was evaporated on the free surface of the PC membrane after electrodeposition. FMR measurements were performed at room temperature at a constant frequency in the range of 100 MHz to 50 GHz, by sweeping the magnetic field applied in the OOP direction from 10 kOe down to zero field. The experimental setup for magneto-transport is based on a four/two-probe measurement system. A mechanical mask was used for selective local removal of Cu cathode by wet chemical etching using the iodine-based solution and for creating an electrode design at the surface of the filled template [Fig. 1(c)]. In this configuration, the current is directly injected to the branched CNW structure from unetched sections of the Cu cathode, thanks to the high degree of electrical connectivity of the CNWs.

It should be noted that the results obtained by four- and two-probe measurements were the same, as the typical resistance values of the prepared specimens (in the range of few tens of Ω) were usually much larger than the ones attributed to the corresponding leads and contacts to the sample. The measured samples were about 1 cm long and the electrical contacts were directly made by Ag paint. For each sample, the input power was kept below 0.1 μW to avoid self-heating, and the resistance was measured within its ohmic resistance range with a resolution of one part in 10^5. The magneto-transport measurements were performed while sweeping a magnetic field between ±10 kOe in the IP and OOP directions. The magneto-transport measurements in this study were made in the temperature range from 20 K to 300 K

III. RESULTS AND DISCUSSION

Figs. 2(a) and 2(b) show SEM micrographs at different magnifications of the self-standing 40 nm diameter NiFe CNW networks after the complete dissolution of the PC template. As expected, the obtained structure exhibits a complex branching structure, imposed by the 3D nanoporous template (see Fig. 1). The interconnected NiFe CNWs provided a high degree of electrical connectivity and good mechanical stability, as the entire 3D-CNW networks (with an area of ~1 cm^2) freed-up from the polymer nanoporous host are self-supported and could be easily handled by tweezers, as seen in the inset of Fig. 2(a). The topological structure of the porous membranes described in Fig. 1 is a key feature in giving rise to robust network architectures made up of self-standing magnetic CNW networks. As seen from Fig. 2(b), the orientation of the cylindrical wires is homogeneous along the angular range of ±45°.

X-ray diffraction has been done in order to analyze the crystallographic and structural properties of the Co CNWs.

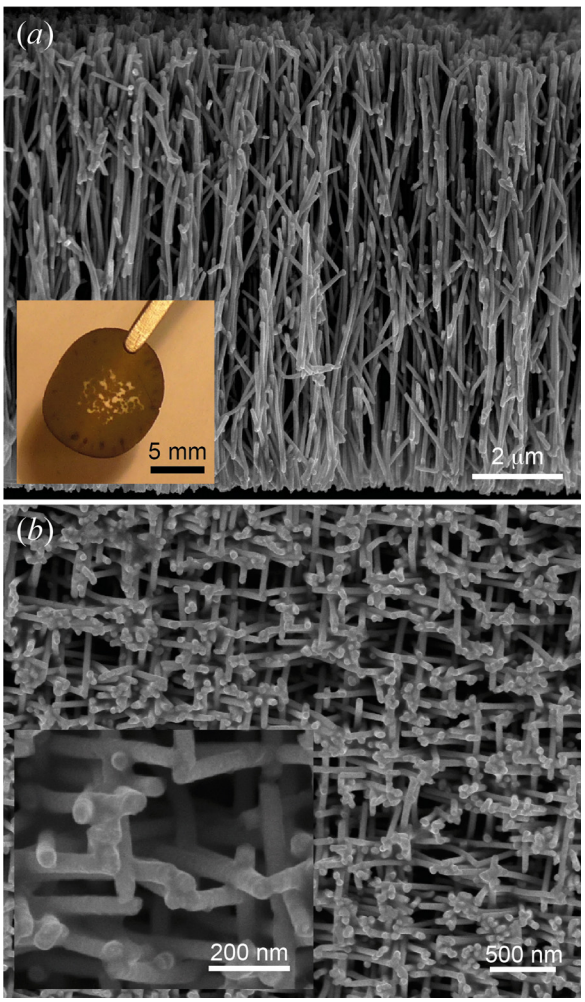

FIG. 2. (a) Low-magnification tilted view SEM image of the interconnected network of electrodeposited 3D NiFe CNWs obtained after the complete dissolution of the PC nanoporous host with an inset optical image showing the mechanical robustness of the macroscopic self-supporting network. (b) High-magnification top view of the dense NiFe CNW network with diameter of 40 nm. The inset displays a close magnification where the low roughness of the nanowires can be appreciated.

Fig. 3 shows the x-ray diffraction patterns of the Co CNWs deposited at (a) pH 2.0, (b) pH 3.6, (c) pH 5.0, and (d) pH 6.4. Overall, comparing the different spectra, clear structural changes can be appreciated as the pH increases from 2.0 to 6.4. For the pH 2.0 sample, the spectra show five peaks. Three of them correspond to the diffraction of (100), (002), and (101) planes of the Co hcp structure. While the strongest peak is that related to the fcc (111) plane and at the right side corresponds to the fcc (200) plane.[22] This confirms that the Co CNWs grown in an electrolyte at a pH value of 2.0 show no favorable structural texture. However, for intermediate pH values, 3.6 and 5.0, in Figs. 3(b) and 3(c), respectively, the strongest peak corresponds to the hcp (100) plane. As the pH is increased from 3.6 to 5.0, the fcc (111), (200) as well as the hcp (200) peak intensity decreases, and for the pH 5.0 sample, the hcp (002) peak vanishes. The hcp (101) peak intensity also increases as the pH is increased from 2.0 to 5.0. This indicates that for the pH interval between 3.6 and 5.0, the hcp Co is predominantly oriented perpendicular to the nanowires axis and the presence of the fcc (111) peak suggests the presence of stacking faults.[22,23] Furthermore, the absence of the hcp (002) peak for the pH 5.0 Co sample implies that for this sample, the texture of the hcp *c*-axis perpendicular to the nanowire axis is of better quality than the pH 3.6 sample. When the pH is increased to 6.4, it can be seen in Fig. 3(d) that a strong texture change takes place. In this case, only the Co hcp (002) peak is observed, along with a small reflection from the fcc (111) plane. This is consistent with a high orientation of the *c*-axis along the nanowires axis. A further quantitative analysis about the grain size-distribution has been derived from the widths of the main peaks using the Scherrer equation for each CNW network. This analysis reveals grain sizes in the range from about 17 to 34 nm, which are lower than the NWs diameter of 40 nm. The specific grain size values extracted from the more intense peaks for each sample are indicated in Fig. 3.

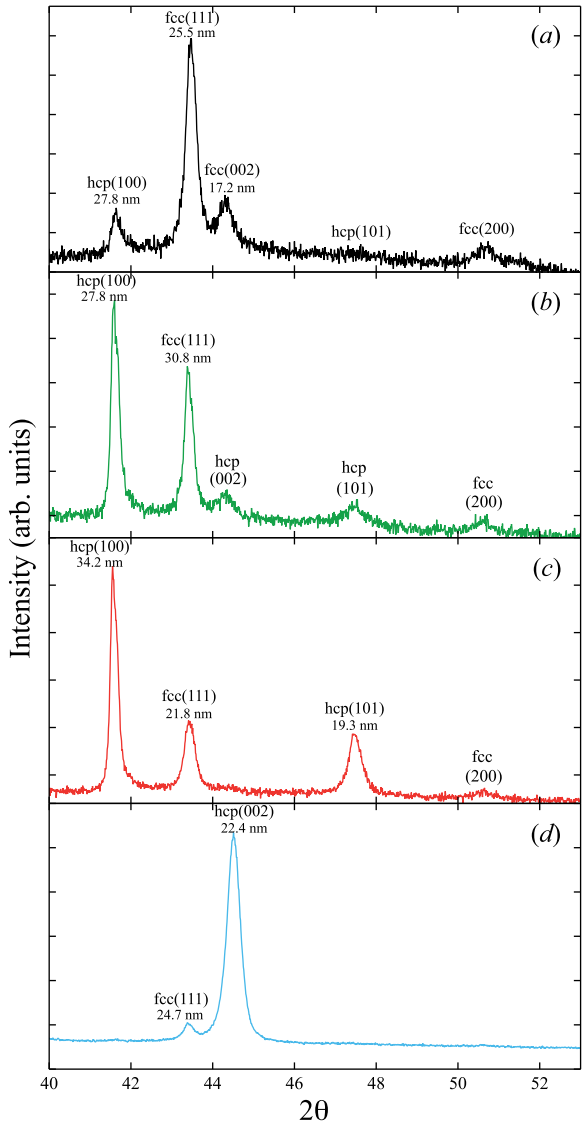

FIG. 3. X-ray diffraction patterns of the Co CNW networks deposited at (a) pH 2.0, (b) pH 3.6, (c) pH 5.0, and (d) pH 6.4. The grain size for the more intense crystal diffraction peaks is displayed in the figure.

Hysteresis loops have been measured at room temperature on the various ferromagnetic CNW networks with the field applied in the OOP and IP directions. Figs. 4(a) and 4(b) show the hysteresis loops measured in both directions for the case of NiFe and Co (pH 2.0) CNWs, respectively. Although exchange interactions at the crossing points of the branched structure and dipolar interactions provide significant contributions to the

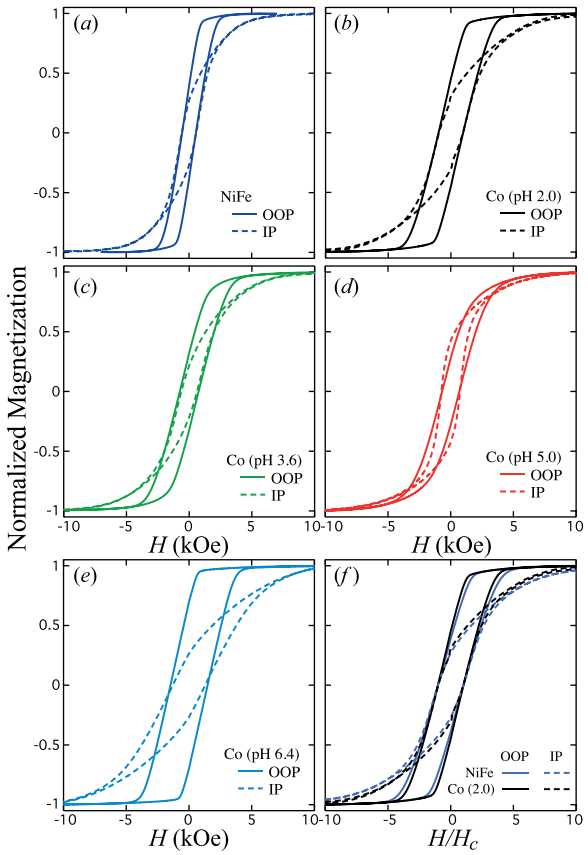

FIG. 4. Hysteresis loops measured with the external field applied out of the plane (OOP) and in the plane (IP) of the PC membrane in (a) NiFe and of electrodeposited Co CNW networks using different electrolytic bath acidities: (b) pH 2.0, (c) pH 3.6, (d) pH 5.0, and (e) pH 6.4. (f) Comparison between the IP and OOP hysteresis loops for the NiFe and Co (pH 2.0) CNW networks of (a) and (b) plotted vs. the field ratio H/H_c, where H_c is the corresponding coercive field.

energy terms, the most dominant energy contribution for our NiFe and Co (pH 2.0) CNW networks is magnetostatic (MS) anisotropy energy, as will be shown afterwards. Figs. 4(b)–4(e) show a comparison of the hysteresis loops measured for Co CNW grown by varying pH value of the electrolytic bath. As seen from these figures, Co CNWs display different magnetic and structural properties by an appropriate choice of pH. Considering the Co CNWs prepared at pH 2.0, as shown by the XRD results (Fig. 3(a)), no hcp texture is present in this sample. Therefore, there is no MC contribution, and the effective anisotropy should be entirely magnetostatic as in the NiFe CNWs. Indeed, comparing the hysteresis loops of this pH 2.0 sample with those for the NiFe sample, shown in Figs. 4(a) and 4(b), the same overall features are observed in both OOP and IP measurements. In contrast, clear differences are observed at higher pH values. In particular, a very significant reduction of the magnetic anisotropy was found for the Co CNWs prepared at pH values 3.6 and 5.0, which, from the XRD data of Figs. 3(b) and 3(c), have a preferential texture with the hcp *c*-axis perpendicular to the nanowires axis. This results in a competition between MS and MC anisotropies. These changes are accompanied by lower remanence and coercivity in the OOP direction. For the sample prepared at pH 5.0, the decrease in the total anisotropy is even larger, since as evidenced from the XRD, at this pH, the quality of the hcp *c*-axis orientation perpendicular to the nanowire axis is better, and thus, a larger MC anisotropy is expected.

In contrast, a very large increase in the effective anisotropy is observed in the system prepared from the high pH solution (pH 6.4), which, as shown by the XRD in Fig. 3, favors a hcp *c*-axis parallel to the NWs, thus resulting in an additive MC contribution to the total anisotropy field. In this case, the squareness in the OOP direction is also strongly enhanced, which is consistent with the properties expected for low diameter NWs with strong uniaxial magnetic anisotropy. For this particular sample (pH 6.4), the field required to reach saturation magnetization in the IP direction is larger than 10 kOe. As can be seen, there is a significant decrease in the saturation field for Co CNWs grown at pH values of 3.6 and 5.0 compared to the pH 2.0 samples and a clear increase of this field for the sample prepared at pH 6.4. Similarly, the squareness of the $M(H)$ loops in the OOP direction increases as the effective anisotropy field increases from its lowest value (pH 5.0) to its highest (pH 6.4), passing through the case in which no MC contribution is present (pH 2.0), indicating that as a function of the pH, the MC contribution can be eliminated or set to reinforce or compete with the MS effects. These changes in the total anisotropy are also consistent with the variations of both the coercive field (H_c) and remanence magnetization (M_r). The highest H_c value (1460 Oe) is found in the pH 6.4 sample, followed by the pH 2.0 sample (944 Oe), while the lowest value (620 Oe) was observed in the pH 3.6 sample, which is a slightly smaller than the 683 Oe value for the pH 5.0 sample. Whereas the M_r values varied from the highest value of 0.7 (pH 6.4) to 0.44 (pH 2.0), then 0.32 (pH 3.6) to the lowest of 0.28 (pH 5.0).

These relations between pH induced structural changes in Co CNWs and their total magnetic anisotropy are in very good agreement with previous results obtained in arrays of parallel Co NWs.[20] In particular, it was shown that the microstructure of the deposited Co NWs can be set to contain a dominant fraction of the Co-hcp phase with the *c*-axis oriented perpendicular to the NWs, for pH values between 3.5 and 5.5, or parallel to the NWs, for pH values larger than 6.0.[20,24] Furthermore, at a pH value of 2.0, no contribution from the MC anisotropy was found, indicating a lack of texture in the Co microstructure.[20] The effect of the pH on the microstructure of the nanowires is effective despite their non-parallel orientation and the presence of interconnections between them. Therefore, these results show that the key parameter that controls the microstructure of CNW networks is the reduced diameter of the nanowires.

Further information about the magnetic properties of the distinct CNW networks can be obtained from FMR measurements. The effect of the solution pH on the magnetic anisotropy of Co CNWs is clearly observed from both absorption spectra and their corresponding relation dispersions shown in Figs. 5(a) and 5(b). For Co CNW networks, the observed behavior in these figures is very similar to what was reported previously for Co parallel nanowire arrays.[20] That is, the resonance frequencies for the samples with pH 3.6 and 5 are lower than those for the MS case (pH 2.0), which is consistent with the configuration where the *c*-axis is oriented perpendicular to the nanowire axis. Conversely, the higher resonance frequencies observed for the pH 6.4 sample are consistent with the reinforcement of the magnetization along the nanowires' axis by the addition of the MC contribution. These results are in good agreement with what is observed from the hysteresis loops in Figs. 4(c)–4(e) and the XRD results. Although the resonance fields for CNW networks also include the shape anisotropy, they are located at different values in contrast with the case of arrays of parallel nanowires, which is due to their different and particular geometrical characteristics that need to be taken into account.

In order to quantitatively characterize the magnetic properties of the distinct CNW networks, consider the average resonance condition in the OOP configuration of the applied field that accounts for all the nanowires orientations (see Section 1 of the supplementary material)

$$f = \gamma\sqrt{H_r^2 + C_1 H_{eff} H_r + C_2 H_{eff}^2}, \tag{1}$$

where C_1 and C_2 are constants that result from the averaging process. As shown by the straight dotted lines in Fig. 5(b), this equation can be used as a fitting function for the determination of the effective anisotropy field (H_{eff}). Furthermore, the magnetic contributions that dominate the value of H_{eff} can be evidenced from the variation of the $f/(4\pi M_s\gamma)$ ratio vs. the $H/(4\pi M_s)$ ratio, where $4\pi M_s$ is the magnetostatic field for an infinite thin film. For purely MS systems, these ratios are dimensionless since both quantities within them are proportional to M_s and thus of MS nature, so a universal single dependence between them must be obtained. As

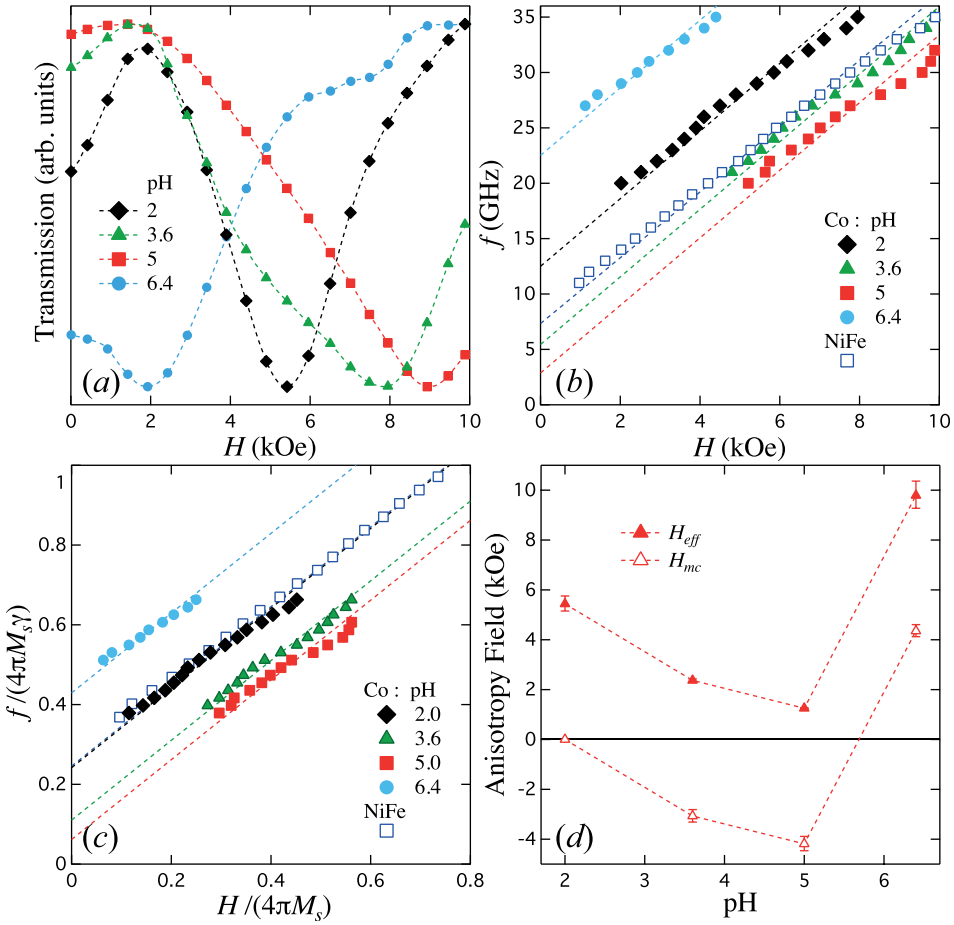

FIG. 5. (a) FMR spectra recorded at 29 GHz on Co CNW networks grown at pH values of 2.0, 3.6, 5.0, and 6.6. (b) Comparison between the dispersion relations for a NiFe CNW network with the corresponding ones for the Co CNW networks of (a). Linear fits shown by the dotted lines are obtained using Eq. (1). (c) Dependence between the $f/(4\pi M_s\gamma)$ and $H/(4\pi M_s)$ ratios for the samples in (b), along with their corresponding dispersion relations (dotted lines) obtained by dividing Eq. (1) by $4\pi M_s\gamma$. (d) Variation of the anisotropy fields H_{eff} and H_{mc} vs. pH for the Co CNW networks of (a). Error bars account for the $\pm 5^\circ$ angular dispersion of the ions bombardment in the track etching process of the PC membrane. Dotted lines are guides for the eye.

shown in Fig. 5(c), the NiFe and Co (pH 2.0) CNW networks fall along the same straight line corresponding to the dependence between the MS ratios, which demonstrates that these networks have only MS contributions. Further evidence of the MS nature of the NiFe and Co (pH 2.0) CNW networks is observed in Fig. 4(f) from the comparison between their IP and OOP hysteresis loops plotted as a function of the H/H_c ratio, with H_c their corresponding coercive field. For purely MS systems, the coercive field is proportional to the saturation magnetization M_s; therefore, the ratio H/H_c is independent on the magnetic material of the nanowires and reflects the same structural factor for all CNW networks. Indeed, the very good agreement between the hysteresis loops for each sample shows that their magnetic behaviors are the same and thus of MS origin. Conversely, when an anisotropy contribution other than the MS one is present, the dependence between the $f/(4\pi M_s\gamma)$ and $H/(4\pi M_s)$ ratios falls bellow or above the MS dependence, as in the case for the Co (pH 3.6) and Co (pH 5), and for Co (pH 6.4) CNW networks, respectively. The decrease (increase) of the ratios dependence with respect to the MS case for the former (later) results from the fact that the c-axis, perpendicular (parallel) to the nanowires, leads to a MC contribution that opposes (reinforces) the MS contribution.

With this in mind, the magnetic origin of the as-obtained H_{eff} field from the extrapolated zero field resonance frequency $[f(H_r = 0) = f_0]$ can be well known. The relationship between f_0 and H_{eff} is obtained directly from Eq. (1) as

$$H_{eff} = \frac{f_0}{\gamma\sqrt{C_2}}, \tag{2}$$

where

$$C_2 = \frac{1}{4}\left(1 + \frac{1}{\theta}\sin 2\theta + \frac{1}{4\theta}\sin 4\theta\right). \tag{3}$$

As shown above, for the case of NiFe and Co (pH 2.0) CNW networks, only MS contributions are present in the anisotropy field, then $H_{eff} = H_{ms}$. However, for the case of Co CNW networks with MC contributions, $H_{eff} = H_{ms} \pm H_{mc}$, so the MC field can be easily determined as $H_{mc} = \pm(H_{eff} - H_{ms})$ by using the previously determined MS field (H_{ms}) for the Co (pH 2.0) sample. In this way, H_{eff} and H_{mc} are obtained using Eq. (2), but with the respective expression for the effective field depending on the CNW network considered under analysis. The effective field for the NiFe and Co (pH 2.0) CNW networks determined using Eq. (2) is, respectively, 3.2 and 5.44 kOe. Since the constant $C_2 < 1$ in this equation, then the corresponding f_0 values for CNW networks are lower than the expected ones for the case of parallel NW arrays that are given by the expression $f_0 = \gamma H_{eff}$.[21] This decrease of f_0 for CNW networks is consistent with the contributions of tilted parallel NW array to different orientations.[15]

Besides, Fig. 5(d) shows the variation of the anisotropy fields H_{eff} and H_{mc} vs. the solution pH for Co CNW networks measured with the external field in the OOP direction. These

fields have been determined using Eq. (2) for $\theta = \pi/4$, where error bars around this angle take into account the $\pm 5^{\circ}$ angular dispersion of the ions bombardment in the track etching process of the PC membrane. The MS field $H_{ms} = H_{eff}$ for the pH 2.0 sample, obtained using Eq. (2), has been used as input parameter into this same equation in order to obtain the corresponding H_{mc} value from H_{eff} for the case of Co CNW networks with pH > 2. As seen in Fig. 5(d), H_{mc} is negative for the samples with pH 3.6 and 5.0 and positive for the pH 6.4 sample, so this field can be tuned in the range from −4.20 to 4.35 kOe, giving rise to a maximum field change of about 8 kOe. Particularly, H_{eff} has the lowest value for the Co (pH 5.0) sample as it is nearly isotropic, in good agreement with its corresponding hysteresis loops shown in Fig. 4(d) and XRD, where it was found that the pH 5.0 sample had the strongest texture with the *c*-axis perpendicular to the nanowires.

Anisotropic magnetoresistance (AMR) measurements constitute another way to investigate the magnetic properties of CNW networks. AMR is due to the anisotropy of spin-orbit scattering in transition ferromagnetic metals and leads to changes in the resistivity as the angle between the directions of the magnetization (M) and current (I) is modified. Despite the fact that the relative change in resistivity between the high resistance state where the magnetization is parallel to the current ($\rho_{||}$) and the low resistance state where the magnetization is perpendicular ($\rho_{\perp}$) is usually small (a few percents or even less), AMR was used in previous works to study the magnetization reversal of magnetic nanowires embedded within templates with parallel pores.[25–27] Fig. 6(a) shows resistance curves measured at different temperatures in the range of 20 K to 300 K with the external field in the OOP (continuous lines) and IP (dashed lines) directions for interconnected NiFe CNW networks with only MS contribution to the magnetic anisotropy. As seen, the maximum resistance is reached near zero applied magnetic field for both directions for all temperatures, which is consistent with remanent magnetization states where magnetization tends to be aligned with the nanowires axis due to the shape anisotropy. Such a parallel configuration between current paths and local magnetization within the nanowire network gives rise to a high resistance state. In the saturated state of either IP or OOP directions, the uniform distribution of nanowire orientations with respect to the normal plane of the membrane leads to a uniform distribution of angles between current paths and magnetization direction at saturation. In that case, resistance measurements correspond to the average magnetoresistive value resulting from the contributions of all the nanowires with different orientations with respect to the applied field direction. Therefore, the resistance states at saturation ($\bar{\rho}_{ip}$ and $\bar{\rho}_{oop}$) in both IP and OOP directions reach values which are intermediate between $\rho_{||}$ and $\rho_{\perp}$, with obviously $\bar{\rho}_{oop}$ larger than $\bar{\rho}_{ip}$ given the characteristics of the membrane pore structure. The same feature is observed for the fcc-like Co CNW network which has only MS contributions, so that $\rho_{||} = \rho(H = 0)$ by analogy with the NiFe

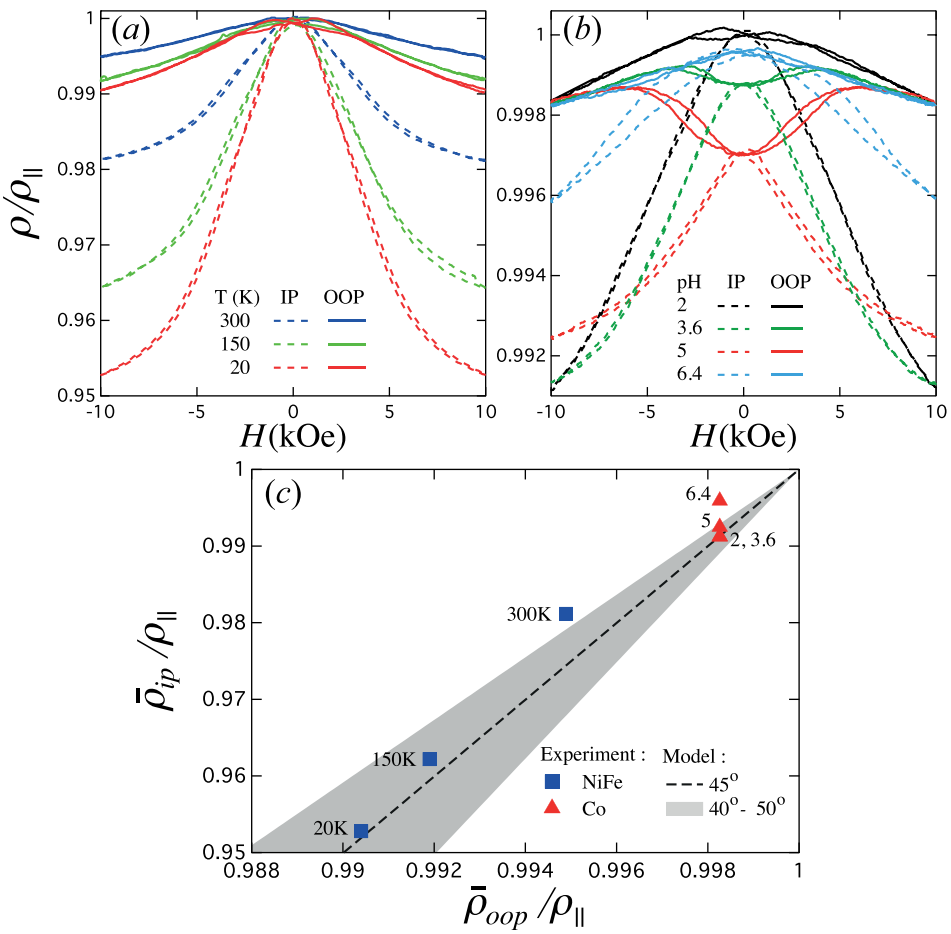

FIG. 6. (a) AMR curves for NiFe CNW networks measured at different temperatures by applying the external field in the OOP (continuous lines) and IP (dashed lines) directions. (b) Room temperature AMR curves for Co CNW networks fabricated from electrolytic solutions with different pH: 2.0, 3.6, 5.0, and 6.4. (c) Comparison between the model [Eq. (5)] and the experimental dependence of $\bar{\rho}_{ip}/\rho_{||}$ vs $\bar{\rho}_{oop}/\rho_{||}$ at $H = 10$ kOe for the CNW networks of Figs. 6(a) and 6(b). The grey shaded area represents the calculated $\bar{\rho}_{ip}/\rho_{||}$ in the angle range $40^{\circ} - 50^{\circ}$.

sample, as seen in Fig. 6(b). Since the maximum resistance for the Co CNW networks with MC contributions (pH ≥ 3.6) is not attained at $H = 0$, their respective curves in Fig. 6(b) are plotted after normalization of the resistance at $H = 10$ kOe in the OOP direction, since the Co CNW networks are magnetically saturated in the direction of the applied field and the resistance states are expected to be the same for all Co CNW networks. For pH values of 3.6 and 5.0, the *c*-axis of the hcp-Co CNWs is preferentially oriented perpendicular towards the axis of the wire, thus leading to a strong transverse MC anisotropy. In agreement with the hysteresis loops in Fig. 4, the reduced value of $\rho/\rho_{||}$ at $H = 0$ is a clear signature of a significant magnetization components perpendicular to the nanowires in the remanent state. For the Co CNW network prepared at pH 6.4, a nonzero transverse component is also observed at $H = 0$, despite the fact that at high pH, electrodeposited Co nanowires with the *c*-axis parallel to its axis are predominantly obtained. This particular result is also consistent with FMR data, showing a double peak structure for pH 6.4, as shown in Fig. 5(c). Also, in accordance with the hysteresis loops in Fig. 4(f), the Co CNW network obtained at pH 6.4 did not become magnetically saturated at the maximum applied field in the IP direction.

In order to more quantitatively analyze the magneto-transport properties for the distinct CNW networks shown in Figs. 6(a) and 6(b), a model has been elaborated to account for each AMR contribution due to all the nanowire orientations in the 3D CNW network. Indeed, a quantitative understanding of the magneto-transport behavior of complex and disordered systems like 3D CNW networks is of paramount importance to determining their AMR ratios ($\Delta\rho/\rho$) and resistance states ($\rho_{\perp}$). The details of the model are presented in Section 2 of the supplementary material. In this sense, the AMR ratio of a CNW network is expressed as

$$\frac{\Delta\rho^{[x]}}{\rho} = \frac{\rho_{||} - \rho_{\perp}^{[x]}}{\rho_{av}^{[x]}}, \tag{4}$$

where $x = ip$ (or *oop*) refers to the IP (or OOP) direction, $\rho_{av}^{[x]} = (1/3)\rho_{||} + (2/3)\rho_{\perp}^{[x]}$ is the average magnetoresistance in 3D systems, and $\rho_{\perp}^{[x]}$ is the theoretical resistance state for the perpendicular configuration between *M* and *I*. In addition, the AMR signal can be extracted directly from the measured resistance values $\bar{\rho}_{ip}$ and $\bar{\rho}_{oop}$ at saturation. Since the superscripts (subscripts) $\bar{\rho}_{ip}$ and $\bar{\rho}_{oop}$ in Eq. (4) only indicate the measurement configuration, then $\rho_{\perp}^{[ip]}$ and $\rho_{\perp}^{[oop]}$ are expected to be equal as they represent the same resistance state ($\rho_{\perp}$).

Table I shows the room temperature AMR ratio for the CNW networks determined using Eq. (4) and from the normalized resistivity values at saturation of Figs. 6(a) and 6(b). AMR ratios at temperatures of 300 K, 150 K, and 20 K are shown for the NiFe sample. The $\Delta\rho/\rho$ values for the different CNW networks are consistent with those previously reported in parallel NW arrays[25–28] and the higher values obtained at low temperature for the NiFe sample are consistent with previous film studies.[29] As seen, the values for $\rho_{\perp}^{[ip]}$ and $\rho_{\perp}^{[oop]}$ are very close to each other for most samples in this table, then we also found that their respective expressions [see Eqs. (9) and (14) of the supplementary material] are indeed equivalent and that the same $\Delta\rho/\rho$ can be obtained from the IP and OOP directions. The AMR ratio for the Co CNW network prepared at pH 6.4 is smaller than the ones reported for the other pH values, which is the result of the disagreement between its $\rho_{\perp}^{[ip]}$ and $\rho_{\perp}^{[oop]}$ values. Indeed, for this sample, the MC contribution reinforces the magnetization easy axis along the nanowires, which in turn reinforces the easy magnetization direction of the ensemble along the OOP direction, as seen from the hysteresis loops shown in Fig. 4(f). Therefore, the range of applied magnetic fields was not enough to saturate the magnetization in the IP direction, and $\Delta\rho/\rho$ was underestimated.

TABLE I. Values of the resistance states $\rho_{\perp}^{[oop]}/\rho_{||}$ and $\rho_{\perp}^{[ip]}/\rho_{||}$ determined using Eqs. (9) and (14) of the supplementary material and the respective AMR ratio ($\Delta\rho/\rho$) for NiFe and of Co CNW networks prepared using different electrolytic bath pH.

Sample	$\rho_{\perp}^{[oop]}/\rho_{||}$	$\rho_{\perp}^{[ip]}/\rho_{||}$	*AMR* (%)
NiFe(300 K)	0.9719	0.9770	2.87
NiFe(150 K)	0.9554	0.9584	4.60
NiFe(20 K)	0.9471	0.9481	5.48
Co(2)	0.9904	0.9892	1.08
Co(3.6)	0.9904	0.9893	1.07
Co(5)	0.9904	0.9908	0.92
Co(6.4)	0.9904	0.9950	0.50

Furthermore, the combination of both expressions for $\rho_{\perp}^{[ip]}$ and $\rho_{\perp}^{[oop]}$ then gives the relation between the measured resistance values at saturation $\bar{\rho}_{oop}$ and $\bar{\rho}_{ip}$ [see Eq. (16) of the supplementary material]. Since the expected target maximum polar angle of the nanowires is $\theta = 45^{\circ}$ and the most likely azimuthal orientation of the magnetization in the IP direction with respect to the nanowires lying in the *x*–*z* plane is $\phi = 45^{\circ}$, then for this particular case the relation between $\bar{\rho}_{ip}$ and $\bar{\rho}_{oop}$ writes

$$\bar{\rho}_{ip} = \frac{1}{2}\left(\frac{3\pi + 2}{\pi - 2}\right)\bar{\rho}_{oop} - \frac{1}{2}\left(\frac{\pi + 6}{\pi - 2}\right)\rho_{||}. \tag{5}$$

Equation (5) [or Eq. (17) of the supplementary material] allows to determine the average resistance value in the saturated state along the IP (OOP) configuration from the corresponding value in the OOP (IP) direction. The parallel configuration between *M* and *I* is identified by the maximum value, $\rho/\rho_{||} = 1$, of the normalized resistance curve in the OOP or IP direction. Due to the reduced diameter of the NWs, this configuration is likely to be reached at $H = 0$ in CNW networks without MC anisotropy contributions, which can deviate its magnetization from the easy direction along their axes. However, the presence of MC contributions will not affect the validity of Eq. (5) since a non zero MC contribution is simply changing the resistance (magnetization) state at $H = 0$ and higher fields are required to reach saturation magnetization. Fig. 6(c) shows the comparison between Eq. (5) for the case $\theta = 45^{\circ}$ and $\phi = 45^{\circ}$ (dashed line) and

the experimental dependence of $\bar{\rho}_{ip}/\rho_{||}$ vs $\bar{\rho}_{oop}/\rho_{||}$ at $H = 10$ kOe for the CNW networks of Figs. 6(a) and 6(b). As seen, the experimental values for the NiFe, Co (pH 2.0), Co (pH 3.6), and Co (pH 5.0) samples lie within the shaded area that corresponds to resistance values in the angle range $40^\circ - 50^\circ$, which are calculated using Eq. (16) of the supplementary material, whose mean $\bar{\rho}_{ip}/\rho_{||}$ vs $\bar{\rho}_{oop}/\rho_{||}$ dependence is located at $\theta = 45^\circ$ (dashed line). This is consistent with an angle dispersion of about $\pm 5^\circ$ around the target maximum angle $\theta = 45^\circ$ expected for the CNW networks considered in the present work. The very good agreement between the model and the experiment observed for most CNW networks shows that their magneto-transport properties are consistent with a resistance average performed over all the nanowires orientations. Furthermore, regardless of the complex magneto-resistive behavior at remanence for the Co CNW networks with MC contributions (pH 3.6 and pH 5.0), their behavior in the saturated state is similar to that for NiFe and fcc-like Co CNW networks, which shows that the proposed model can also be used for CNW networks with different anisotropy contributions.

IV. CONCLUSIONS

In this work, we have explored the magnetic and magneto-transport properties of CNW networks fabricated from distinct materials by electrodeposition into the crossed and interconnected nanochannels of track etched polymer membranes. Among the advantages of the interconnected nanowire architecture are its mechanically stable and self-supporting feature after chemical dissolution of the polymer membrane, as well as the ease of carrying out magneto-transport measurements and its direct interplay with their magnetic properties. Control of the electrodeposition conditions, in particular, the electrolytic bath acidity made possible to modify the crystallographic structure of Co CNW networks, which strongly influenced its magnetic anisotropy, microwave absorption, and anisotropic magnetoresistance. The accurate determination of these properties has been possible with the use of proposed analytical models which are based on simple arguments that are consistent with an average performed over all the nanowires orientations of the 3D architecture. The feasibility to obtain considerable AMR signals in CNW networks made them very interesting structures for potential applications of 3D nanowire networks in magnetic memory, sensor, and logic devices. Finally, the present work opens up the possibility for a controlled synthesis of complex nanoarchitectures with tunable magnetic and magneto-transport properties.

SUPPLEMENTARY MATERIAL

See supplementary material for the FMR condition and AMR model for CNW networks.

ACKNOWLEDGMENTS

This work was partly supported by the Fédération Wallonie-Bruxelles (ARC 13/18-052, Supracryst), CONACYT project CB-177896 and the 2015 UNAM-DGAPA-PAPIIT Program project IA102915. Y. Velázquez-Galván acknowledges CONACYT for scholarship 348405. The authors are thankful to Dr. Etienne Ferain and it4ip Company for supplying polycarbonate membranes, as well as to LINAN-IPICYT for access to their facilities and Beatriz Rivera Escoto and Dr. Gladis Labrada for their technical assistance with the XRD and SEM, respectively.

[1]M. Tian, W. Wang, Y. Wei, and R. Yang, J. Power Sources **211**, 46 (2012).
[2]W. Wang, M. Tian, A. Abdulagatov, S. M. George, Y.-C. Lee, and R. Yang, Nano Lett. **12**, 655 (2012).
[3]S. Xiong, C. Yuan, X. Zhang, and Y. Qian, Cryst. Eng. Comm. **13**, 626 (2011).
[4]C. Wei, H. Pang, B. Zhang, Q. Lu, S. Liang, and F. Gao, Sci. Rep. **3**, 2193 (2013).
[5]A. Vlad, V.-A. Antohe, J. M. Martínez-Huerta, E. Ferain, J.-F. Gohy, and L. Piraux, J. Mater. Chem. A **4**, 1603 (2016).
[6]O. S. Kwon, S. J. Park, H. Yoon, and J. Jang, Chem. Commun. **48**, 10526 (2012).
[7]L. Piraux, V.-A. Antohe, E. Ferain, and D. Lahem, RSC Adv. **6**, 21808 (2016).
[8]I. Paulowicz, V. Hrkac, S. Kaps, V. Cretu, O. Lupan, T. Braniste, V. Duppel, I. Tiginyanu, L. Kienle, R. Adelung, and Y. K. Mishra, Adv. Electron. Mater. **1**, 1500081 (2015).
[9]M. Rauber, I. Alber, S. Müller, R. Neumann, O. Picht, C. Roth, A. Schökel, M. E. Toimil- Molares, and W. Ensinger, Nano Lett. **11**, 2304 (2011).
[10]M. R. J. Scherer and U. Steiner, Nano Lett. **13**, 3005 (2013).
[11]E. J. W. Crossland, M. Kamperman, M. Nedelcu, C. Ducati, U. Wiesner, D. M. Smilgies, G. E. S. Toombes, M. A. Hillmyer, S. Ludwigs, U. Steiner, and H. J. Snaith, Nano Lett. **9**, 2807 (2009).
[12]S. Wang, L.-P. Xu, H.-W. Liang, S.-H. Yu, Y. Wen, S. Wang, and X. Zhang, Nanoscale **7**, 11460 (2015).
[13]S. Rahong, T. Yasui, T. Yanagida, K. Nagashima, M. Kanai, A. Klamchuen, G. Meng, Y. He, F. Zhuge, N. Kaji, T. Kawai, and Y. Baba, Sci. Rep. **4**, 5252 (2014).
[14]S. Rahong, T. Yasui, T. Yanagida, K. Nagashima, M. Kanai, G. Meng, Y. He, F. Zhuge, N. Kaji, T. Kawai, and Y. Baba, Sci. Rep. **5**, 10584 (2015).
[15]E. Araujo, A. Encinas, Y. Velázquez-Galván, J. M. Martínez-Huerta, G. Hamoir, E. Ferain, and L. Piraux, Nanoscale **7**, 1485 (2015).
[16]G. Hrkac, J. Dean, and D. A. Allwood, Philo. Trans. R. Soc. London, Ser. A **369**, 3214 (2011).
[17]D. Wang, H. P. Jakobson, R. Kou, J. Tang, R. Z. Fineman, D. Yu, and Y. Lu, Chem. Mater. **18**, 4231 (2006).
[18]J. Martín, M. Martín-González, J. Francisco Fernández, and O. Caballero-Calero, Nat. Commun. **5**, 5130 (2014).
[19]E. Ferain and R. Legras, Nucl. Instrum. Methods Phys. Res. **208**, 115 (2003).
[20]M. Darques, A. Encinas, L. Vila, and L. Piraux, J. Phys. D: Appl. Phys. **37**, 1411 (2004).
[21]A. Encinas, M. Demand, L. Vila, L. Piraux, and I. Huynen, Appl. Phys. Lett. **81**, 2032 (2002).
[22]O. Ducreux, B. Rebours, J. Lynch, M. Roy-Auberger, and D. Bazin, Oil Gas Sci. Technol. **64**, 49 (2009).
[23]J.-L. Maurice, D. Imhoff, P. Etienne, O. Durand, S. Dubois, L. Piraux, J.-M. George, P. Galtier, and A. Fert, J. Magn. Magn. Materi. **184**, 1 (1998).
[24]A. Sklyuyev, M. Ciureanu, C. Akyel, P. Ciureanu, and A. Yelon, J. Appl. Phys. **105**, 023914 (2009).
[25]J.-E. Wegrowe, D. Kelly, A. Franck, S. E. Gilbert, and J.-P. Ansermet, Phys. Rev. Lett. **82**, 3681 (1999).
[26]S. Pignard, G. Goglio, A. Radulescu, L. Piraux, S. Dubois, A. Declémy, and J. L. Duvail, J. Appl. Phys. **87**, 824 (2000).
[27]T. Ohgai, L. Gravier, X. Hoffer, M. Lindeberg, K. Hjort, R. Spohr, and J.-P. Ansermet, J. Phys. D: Appl. Phys. **36**, 3109 (2003).
[28]A. Fert and L. Piraux, J. Magn. Magn. Mater. **200**, 338 (1999).
[29]T. McGuire and R. Potter, IEEE Trans. Magn. **11**, 1018 (1975).